Phase-Field Modeling of Alloy Oxidation at High Temperatures

Rui Wang[1,2], Yanzhou Ji[2], Tian-Le Cheng[1,3], Fei Xue[1,3], Long-Qing Chen[2], You-Hai Wen[1,*]

[1]*National Energy Technology Laboratory, 1450 Queen Avenue Southwest, Albany, Oregon 97321, USA*

[2]*Department of Materials Science and Engineering, The Pennsylvania State University, University Park, Pennsylvania 16802, USA*

[3]*NETL Support Contractor, 1450 Queen Ave SW, Albany, OR 97321 USA*

Abstract

Oxide growth is a complex process involving transport of reactive species, heterogeneous reactions, and microstructure evolution. Predicting oxidation kinetics and especially the oxide morphological change has been a long-standing challenge. Here we develop a phase-field model for predicting the oxide growth kinetics of a multicomponent alloy during high temperature oxidation, focusing on internal oxidation (non-protective) and its transition to external oxidation (protective). The predicted kinetics and oxide morphology are analyzed and compared to the classical Wagner's theory and an existing analytical model by Zhao and Gleeson. Some assumptions used in the analytical models and the limitation are discussed. In addition, it is demonstrated that the morphology and distribution of the initial oxide nuclei play an important role in the later stage oxide connectivity and thus the transition to external oxidation.

Key words: phase-field method, oxidation, alloys, internal oxidation, external oxidation

* Corresponding author. Email: Youhai.Wen@netl.doe.gov

1 Introduction

High temperature applications of metallic alloys rely on the spontaneous formation of a dense, protective surface oxide layer from rapid oxidation, and thus our ability to predict and control the oxide morphology is of great importance for the design of structural alloys. During the past few decades, extensive experimental efforts have been devoted to investigating the formation mechanism and growth behavior of the protective oxide layers in a number of structural alloys, especially Fe-based [1-8] and Ni-based alloys [7, 9-13]. It has been known that: (1) The alloy composition is one of the crucial factors for the formation of protective layers [8, 9, 14, 15] which may be tuned to provide external oxidation as opposed to the internal (non-protective) oxidation, and achieving the transition from internal to external oxidation is a key objective for the design of high temperature alloys [8]; (2) The formation of the protective oxide layer depends on temperature, defect species present in an alloy, etc., although there has no general agreement on its formation mechanism for specific alloys [9, 15-18]; (3) The rate limiting process for oxidation is mostly the inward and/or outward diffusion of the reactants.

There have also been extensive theoretical studies on the internal/external oxidation mechanisms [8, 14, 19-23]. The best known theory is the Wagner's theory of internal oxidation [14] in which the volume fraction of oxide f_v is determined by diffusion of reacting components and their boundary compositions. Although Wagner directly linked material parameters to the internal-to-external oxidation transition, the volume fraction f_v was assumed to be a constant. Zhao et al. [23] improved Wagner's model and replaced the constant oxygen diffusivity by the effective diffusivity of the metal/oxide system as a function of f_v, so that f_v can evolve as the oxide film grows. A critical volume fraction f_v^* was then derived to determine whether an alloy with certain diffusivities and boundary composition values would eventually form a continuous layer.

Both Wagner's and Zhao's models, due to their analytical nature, largely ignored the detailed microstructures of the internal oxidation zone (IOZ) that can have a major impact on the kinetic process.

The kinetic process of oxidation is always accompanied with complex microstructure evolution. There have been recent attempts [20-22, 24] to apply the phase-field method (PFM) [25] to model and predict the diffusion-reaction processes as well as the corresponding microstructure evolution during high temperature oxidation. For example, the charge interaction and its effect on oxidation kinetics was investigated using the phase-field method [20, 22]. In order to resolve the space charge region, the total length scale of these models is limited by the so-called Debye screen length which is typically on the order of 10^{-8}-10^{-7} m in many oxides with a few exceptions [16]. In principle, the influence of charge interaction on ionic diffusion beyond the Debye length scale can be effectively incorporated by adopting the so-called ambipolar diffusion coefficient as a reasonable approximation [26], which can significantly reduce the computation cost. Most of these existing investigations have been focused on one-dimensional (1D) systems with ideal or regular solution thermodynamic descriptions (e.g., Al, O, electron and holes). Here we develop and implement a phase-field model to predict the oxidation kinetics and the morphology of the internal oxide particles and external layers based on a phase-field model of stoichiometric reactions and solid solutions [27-29]. It incorporates the most relevant diffusion and reaction mechanisms such as inward diffusion of oxygen and outward diffusion of metal atoms, simultaneous growth of more than one oxide such as a Al_2O_3 and NiO in a Ni-Al alloy system with different growth rates, as well as the competition among the diffusion and reaction processes. It also allows direct incorporation of thermodynamic database rather than relying on simplifying assumptions such as ideal or regular solution models.

Table 1: The description for parameters that are used in the model.

Parameter	Description	Values or expressions
ξ	A_2O_3 order parameter	$0 \le \xi \le 1$
ϕ	BO order parameter	$0 \le \phi \le 1$
c_{A}	A composition in the matrix phase	$0 \le c_A \le 1$
c_A^0	Initial A composition	$0 \le c_A^0 \le 1$
c_{O}	O composition in the matrix phase	$0 \le c_O \le 1$
c_S	Oxygen composition at surface	$0 \le c_S \le 1$
μ_{X}	Chemical potential of species X in the matrix phase	Taken from database [30]
$\mu_{\mathrm{X}}, \mu^{\gamma}$	Chemical potential of oxide X, and matrix phase (γ)	Taken from database [30]
κ_ξ, κ_ϕ	Gradient energy coefficients	$\kappa_\xi = \kappa_\phi = 3.54 \times 10^{-8}$ J/m
g	Double well potential	$g(\phi,\xi) = \phi^4 - 2\phi^3 + \phi^2 + \xi^4 - 2\xi^3 + \xi^2 + 50\phi^2\xi^2$
h	Interpolation function	$h(x) = 6x^5 - 15x^4 + 10x^3$
$M_{\mathrm{A}}^{\gamma}, M_{\mathrm{O}}^{\gamma}$	Diffusion mobility of A and O in γ phase	$M_{\mathrm{A}}^{\gamma} = 1.6 \times 10^{-19}$ m^5/(J·s) $M_{\mathrm{O}}^{\gamma} = 6 \times 10^{-18}$ m^5/(J·s)
$M_{\mathrm{O}}^{\mathrm{A_2O_3}}, M_{\mathrm{O}}^{\mathrm{BO}}$	Diffusion mobility of O in A_2O_3 and BO phase	$M_{\mathrm{O}}^{\mathrm{A_2O_3}} = 6 \times 10^{-20}$ m^5/(J·s) $M_{\mathrm{O}}^{\mathrm{BO}} = 3 \times 10^{-18}$ m^5/(J·s)
w	Height of double well potential	8.58×10^8 J/m^3
V_m	Molar volume of the matrix	1.06×10^{-5} m^3/mol
L_ξ	Linear reaction coefficient for A_2O_3	5×10^{-8} m^3/(J·s)
L_ϕ	Linear reaction coefficient for BO	5×10^{-7} m^3/(J·s)
$\widetilde{\mu_{\mathrm{O}}^{\gamma}}, \widetilde{\mu_{\mathrm{A}}^{\gamma}}$	Diffusion potential of O, A and B in γ phase	Taken from database [30]

2 Phase-field model of oxidation

For simplicity, we start with a hypothetical binary alloy A-B with A_2O_3 and BO as the only possible oxides. Without loss of generality, we assume that A_2O_3 is thermodynamically more stable than BO. The total free energy of an inhomogeneous microstructure consisting of A-B alloy and oxides A_2O_3 and BO is expressed as a functional of the phase-field variables $c_{\mathrm{A}}, c_{\mathrm{O}}, \xi, \phi$, given by

$$F = \int_V \left\{ w \cdot g(\xi,\phi) + \frac{1}{2}\kappa_\xi(\nabla\xi)^2 + \frac{1}{2}\kappa_\phi(\nabla\phi)^2 + \frac{1}{V_m}\left[h(\xi)\cdot\mu_{\mathrm{A_2O_3}} + h(\phi)\cdot\mu_{\mathrm{BO}} + \left(1-h(\xi)-h(\phi)\right)\cdot\mu^\gamma(c_{\mathrm{O}},c_{\mathrm{A}})\right]\right\} dV \quad (1)$$

where the definitions of all variables and parameters are listed in Table 1. In equation (1), the first three terms describe the interfacial energy between the different phases. The terms $\mu_{\mathrm{A_2O_3}}$ and μ_{BO} represent the chemical potentials of the corresponding oxides while the last term is the chemical potential of the matrix phase. In this model, the oxides are considered stoichiometric so that $\mu_{\mathrm{A_2O_3}}$ and μ_{BO} are constants under a given temperature while $\mu^\gamma(c_O, c_{\mathrm{A}})$ is a function of composition in the matrix phase. For these chemical potentials, we adopt the thermodynamic database of the Al-Ni-O system by Ross *et al*. [30]. The original $\mu^\gamma(c_O, c_{\mathrm{A}})$ in the Al-Ni-O database is calculated from a sublattice model by assuming a regular solution consisting of A, B and O atoms, where up to three orders of mixing terms are included. In the A-B-O system, the mixing entropy terms of $\mu^\gamma(c_O, c_{\mathrm{A}})$ are removed for simplicity (see supplemental material for details), and then the model can be quantitatively compared with existing analytical models where diffusion equations are expressed based on Fick's law [14, 23]. Since the Al_2O_3 is very stable with an extremely low equilibrium oxygen composition $c_{\mathrm{O}}^{\mathrm{eq}} < 10^{-12}$ [31] in the matrix, $\mu_{\mathrm{A_2O_3}}$ is designed slightly larger than that of Al_2O_3 in order to ensure the equilibrium compositions of A and O in the matrix phase fall within the region range of 10^{-4}-10^{-3} for the sake of computational robustness.

Based on the reaction framework developed in [27-29], the governing evolution equations for the phase and concentration fields are

$$\frac{\partial \xi}{\partial t} = -L_\xi \frac{\delta F}{\delta \xi} = -L_\xi \left[w \frac{\partial g}{\partial \xi} - \kappa_\xi \nabla^2 \xi + \frac{1}{V_m} \frac{\partial h}{\partial \xi} \left(\frac{1}{5} \mu_{\mathrm{A_2O_3}} - \frac{2}{5} \mu_{\mathrm{A}}^{\gamma} - \frac{3}{5} \mu_{\mathrm{O}}^{\gamma} \right) \right] \tag{2}$$

$$\frac{\partial \phi}{\partial t} = -L_\phi \frac{\delta F}{\delta \phi} = -L_\phi \left[w \frac{\partial g}{\partial \phi} - \kappa_\phi \nabla^2 \phi + \frac{1}{V_m} \frac{\partial h}{\partial \phi} \left(\frac{1}{2} \mu_{\mathrm{BO}} - \frac{1}{2} \mu_{\mathrm{B}}^{\gamma} - \frac{1}{2} \mu_{\mathrm{O}}^{\gamma} \right) \right] \tag{3}$$

$$\frac{\partial c_O}{\partial t} = \nabla \cdot M_{\mathrm{O}}(\xi, \phi) \nabla \widetilde{\mu_{\mathrm{O}}^{\gamma}} - \frac{\partial}{\partial t} \left[h(\xi) \left(\frac{3}{5} - c_O \right) \right] - \frac{\partial}{\partial t} \left[h(\phi) \left(\frac{1}{2} - c_O \right) \right] \tag{4}$$

$$\frac{\partial c_{\mathrm{A}}}{\partial t} = \nabla \cdot M_{\mathrm{A}}(\xi, \phi) \nabla \widetilde{\mu_{\mathrm{A}}^{\gamma}} - \frac{\partial}{\partial t} \left[h(\xi) \left(\frac{2}{5} - c_A \right) \right] + \frac{\partial h(\phi) c_A}{\partial t} \tag{5}$$

In equations (4) and (5), we use an interpolation function for the mobility of A and O at the oxide-alloy interface and inside the oxides. For example, the local oxygen mobility is expressed as

$$M_{\mathrm{O}}(\xi, \phi) = [1 - h(\xi) - h(\phi)] M_{\mathrm{O}}^{\gamma} + h(\xi) M_{\mathrm{O}}^{\mathrm{A_2O_3}} + h(\phi) M_{\mathrm{O}}^{\mathrm{BO}} \tag{6}$$

and the A mobility can be expressed in a similar way. The values of M_{O}^{γ}, $M_{\mathrm{O}}^{\mathrm{A_2O_3}}$, and $M_{\mathrm{O}}^{\mathrm{BO}}$ in equation (6) can be found in [32]. In Equations (2) and (3),

$$\Delta \mu_{\mathrm{A_2O_3}} = \frac{1}{5} \mu_{\mathrm{A_2O_3}} - \frac{2}{5} \mu_{\mathrm{A}}^{\gamma} - \frac{3}{5} \mu_{\mathrm{O}}^{\gamma}$$

and

$$\Delta \mu_{\mathrm{BO}} = \frac{1}{2} \mu_{\mathrm{BO}} - \frac{1}{2} \mu_{\mathrm{B}}^{\gamma} - \frac{1}{2} \mu_{\mathrm{O}}^{\gamma}$$

are the chemical potential changes for the oxidation reactions leading to the formation of oxide $\mathrm{A_2O_3}$ and BO, respectively. We define the driving forces for oxidation as $DF_{\mathrm{A_2O_3}} = -\Delta \mu_{\mathrm{A_2O_3}}$ and $DF_{\mathrm{BO}} = -\Delta \mu_{\mathrm{BO}}$.

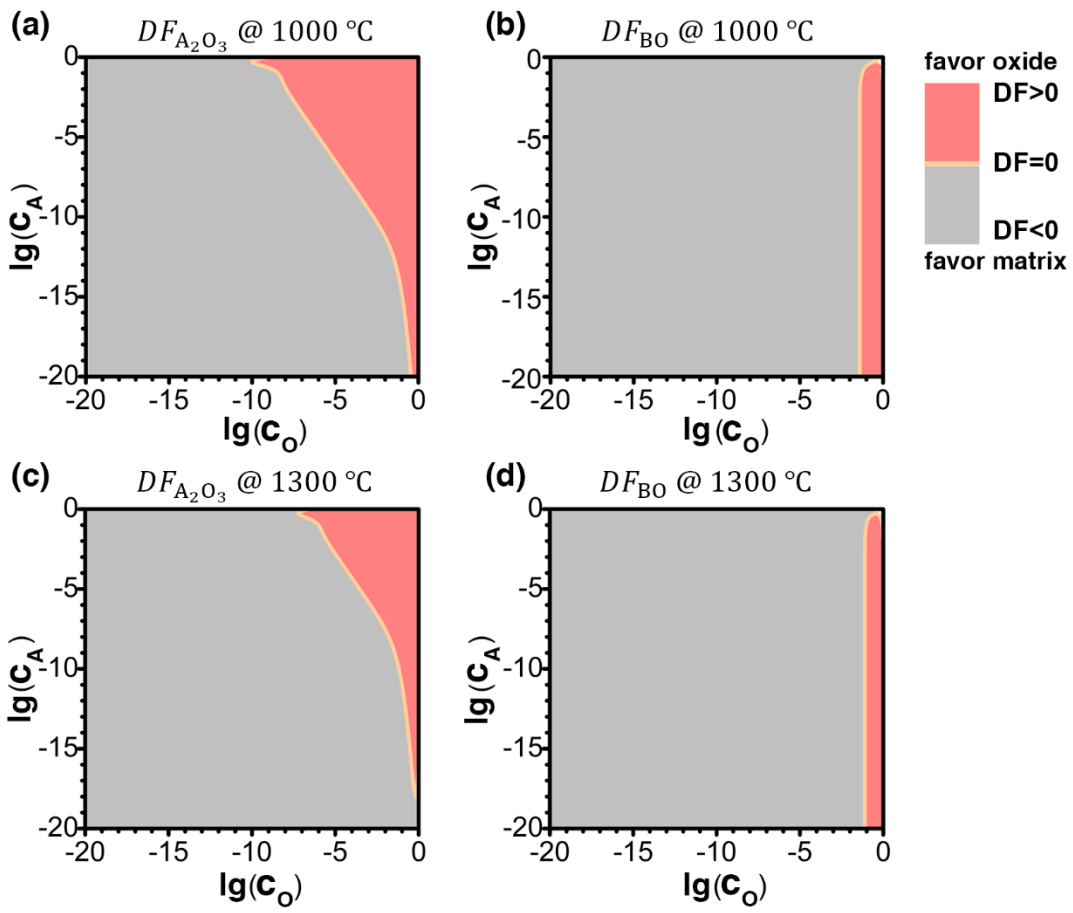

Figure 1: Driving forces for oxidation $DF_{A_2O_3}$ and DF_{BO} plots with respect to composition of A and O for A_2O_3 and BO at 1000 ℃ and 1300 ℃. The orange area indicates that the corresponding oxidation reaction driving force is positive, where the formation of the corresponding oxide is favored. On the other hand, the grey area has a negative driving force, so the matrix phase is favored.

We plot the values of $DF_{A_2O_3}$ and DF_{BO} as functions of compositions of A and O at different temperatures in Figure 1. The orange and grey areas indicate that the corresponding driving forces are positive (oxidation reaction favored) and negative (reduction reaction favored), respectively. According to Figures 1 (a) and (b), the A_2O_3 has a much larger stability range than BO in terms of

the composition of A (or B) and O, indicating A_2O_3 is thermodynamically more stable than BO. In the following sections, we assume that the environmental oxygen partial pressure is above the equilibrium partial pressure for oxidizing A, but it is below the equilibrium partial pressure for oxidizing B.

Below is the procedure to perform a phase-field simulation of oxidation:

1. Assign $c_{\mathrm{A}}, c_{\mathrm{O}}, \xi, \phi$ as the phase-field variables representing the A composition, O composition, A_2O_3 phase and BO phase, respectively. All these variables range from 0 to 1, $c_{\mathrm{A}}(\mathbf{r})$ and $c_{\mathrm{O}}(\mathbf{r})$ are the atomistic composition at position $\mathbf{r}$. $\xi(\mathbf{r}) = \phi(\mathbf{r}) = 0$ indicates the A-B matrix at position $\mathbf{r}$, $\xi(\mathbf{r}) = 1, \phi(\mathbf{r}) = 0$ and $\xi(\mathbf{r}) = 0, \phi(\mathbf{r}) = 1$ represent A_2O_3 and BO phases at position $\mathbf{r}$, respectively. The interfaces are categorized as regions with $0 < \xi(\mathbf{r}) < 1$ and $0 < \phi(\mathbf{r}) < 1$.
2. Calculate the chemical potentials of A, B and O based on the existing thermodynamic database and the updated profiles of c_{A} and c_{O}.
3. Based on the oxidation reactions: $\frac{2}{5}\mathrm{A} + \frac{3}{5}\mathrm{O} \rightarrow \frac{1}{5}\mathrm{A_2O_3}$ and $\frac{1}{2}\mathrm{B} + \frac{1}{2}\mathrm{O} \rightarrow \frac{1}{2}\mathrm{BO}$, determine the evolution of ξ and ϕ based on the reaction driving forces $DF_{\mathrm{A_2O_3}} = -\Delta\mu_{\mathrm{A_2O_3}}$ and $DF_{\mathrm{BO}} = -\Delta\mu_{\mathrm{BO}}$. The reaction rate is assumed linearly proportional to the chemical potential difference according to linear kinetic theory.
4. Based on the calculated reaction rates, determine the evolution of c_{A} and c_{O} by solving the diffusion-reaction equations derived from the thermodynamic framework, Equations (4) and (5).
5. Update the profiles $c_{\mathrm{A}}, c_{\mathrm{O}}, \xi, \phi$ and go back to step 2 until desired simulation time.

In the simulations, the evolution equations (Equations (2)-(5)) are solved following forward Euler's method where the simulation can be greatly accelerated within Message Passing Interface

(MPI). In addition, the reaction evolution equations, i.e., Equations (2) and (3), are evolved until equilibrium after diffusion equations, i.e., Equations (4) and (5), so that the diffusion-controlled oxidation processes are ensured.

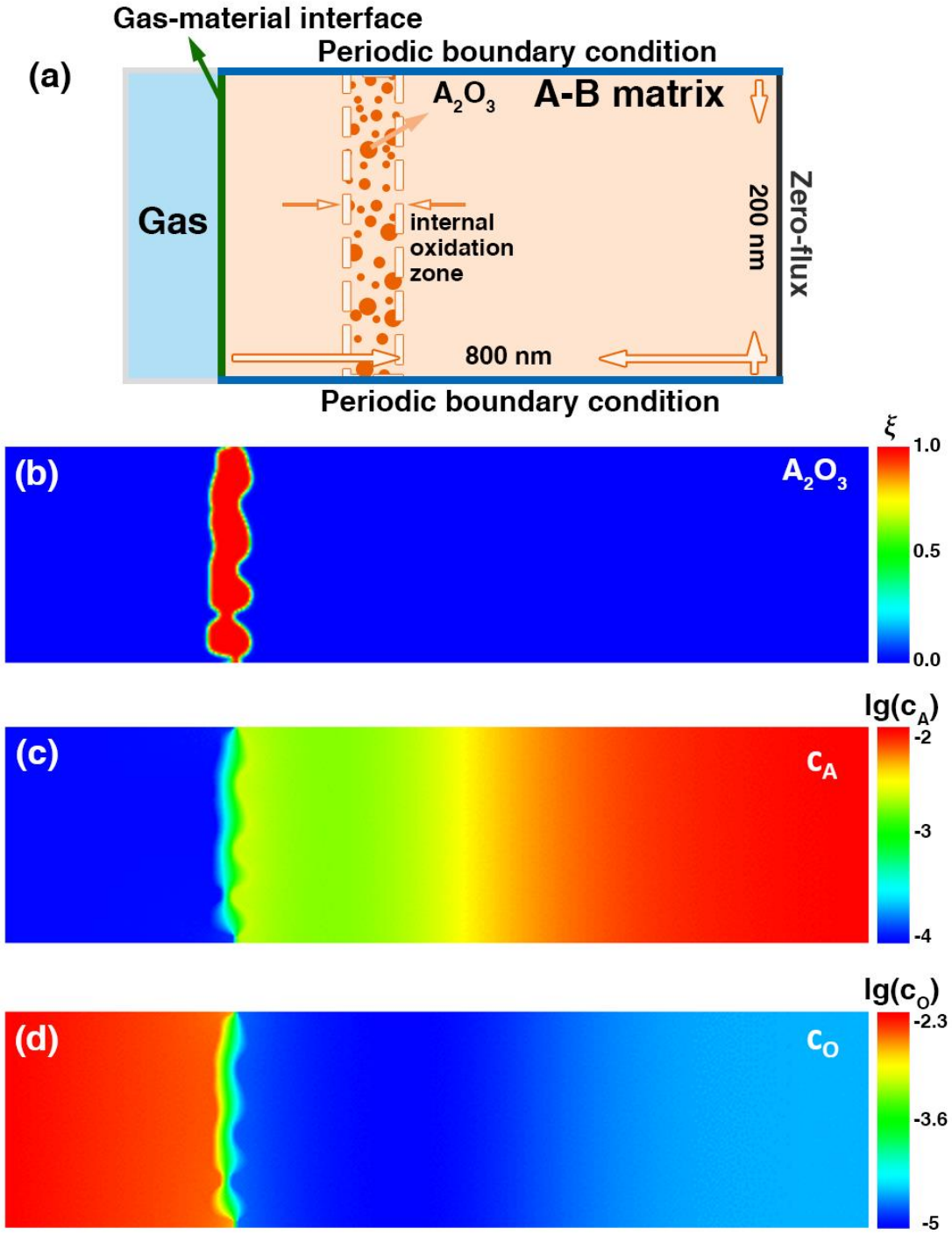

Figure 2: A 2D simulation example of A-B alloy by this model. (a) Simulation setup, in this demonstration, round nuclei with random radii and distributions in an internal oxidation zone are inputted in the simulation system, with initial A composition depleted near the gas-material interface and $c_{\mathrm{A}}^{0} = 0.1$ in the matrix. (b)-(d) profiles of A_2O_3 (in red), c_{A} and c_O at t=200 s, respectively.

3 Phase-field Simulations

Figure 2 (a) shows one possible setup of the simulation. The simulated system includes the oxide phases and the matrix, while the oxygen (gas) phase is not directly considered. The Dirichlet boundary condition for c_{O} is applied at the left boundary of the system (Labeled in green color in Figure 2 (a)), which describes an equilibrium oxygen concentration at the gas-material interface c_S. The value of c_S is a function of oxygen partial pressure in the environment by assuming the dissociation of O_2 $O_2 \rightarrow 2O$ is fast and reaches equilibrium at the left boundary. Zero-flux boundary condition is applied to the right boundary, while periodic boundary conditions are applied to the upper and lower boundaries of the system.

First, we consider an exemplary simulation with the initial condition of randomly distributed A_2O_3 nuclei located inside a designed internal oxidation zone. Figure 2 (b) shows the oxide distribution at t=200 *s*, where a layer of A_2O_3 already forms near the IOZ. The composition c_{A} is depleted on the left side of the A_2O_3 layer, as demonstrated in Fig. 2(c), which indicates that the A atoms are consumed by the oxidation. The oxygen concentration c_{O} significantly drops on the right side of the A_2O_3 layer, as shown in Fig. 2(d), which is caused by the blocking effect of the oxide.

3.1 Comparison with predictions from Wagner's theory

In 1950s, Wagner proposed that the thickness of the oxide film should follow a parabolic growth law $l = k\sqrt{D_O t}$ based on the assumption that the oxygen diffusion is the rate-limiting process[14], while the coefficient k is determined by solving the couple-flux equation at the oxidation front, i.e. the flux of reactant metal and oxygen at the interface should match the stoichiometric ratio of the oxide. As a result, the volume fraction of the oxide in the internal oxidation zone can be predicted from Wagner's theory by calculating the ratio between the flux of the components at the oxidation front and the thickening rate of the oxide. Although the details of the oxide morphology and the evolution inside the internal oxidation zone are neglected, Wagner's theory provides the value of the oxide volume fraction for the internal oxidation process at the steady state as a function of diffusivities and initial compositions. In our current model, most of the assumptions can be kept or lifted as the evolution equations (i.e. Equations (2) and (3) in Section 2.1) naturally consider the coupling of diffusion and reaction processes without assuming an instantaneous reaction as in Wagner's theory. The reaction rate in our model is determined by both the reaction coefficient L and the reaction driving force.

To validate our model, we first simulated the oxidation process by keeping the assumptions in Wagner's theory. In this simulation, we proposed an A-B alloy with A being the only reactive component with oxygen to form an oxide A_2O_3, and we analyze the same situation based on Wagner's theory. A 10 nm layer of A_2O_3 with a uniform profile of $c_A^0 = 0.1$ and a depleted $c_O^0 = 0.001$ is initially set in a 1D system with number of grid points nx=1600 and mesh size Δx=5 nm each, as illustrated in Fig. 3(a). The oxidation rate from our simulation matches well with Wagner's analytical model, as shown in Figure 3 (b). Figures 3 (c) and (d) show the profile of c_A, c_O and the order parameter ξ representing the oxide A_2O_3 at t=50 and t=400, respectively. The analytical

solutions of theses profiles are also plotted. As shown in Figures 3 (b)-(d), the profiles show good agreement with Wagner's theory, whereas the most notable discrepancies come from the composition profile near the reaction front and within the IOZ. This is because Wagner's theory assumes an instantaneous reaction at the oxidation front while taking the equilibrium composition of both components as zero. On the other hand, the oxidation rate in the phase-field model depends on the local chemical potential of oxygen and component A. As a result, the equilibrium compositions must be finite, which would then lead to the finite compositions beyond the oxidation front.

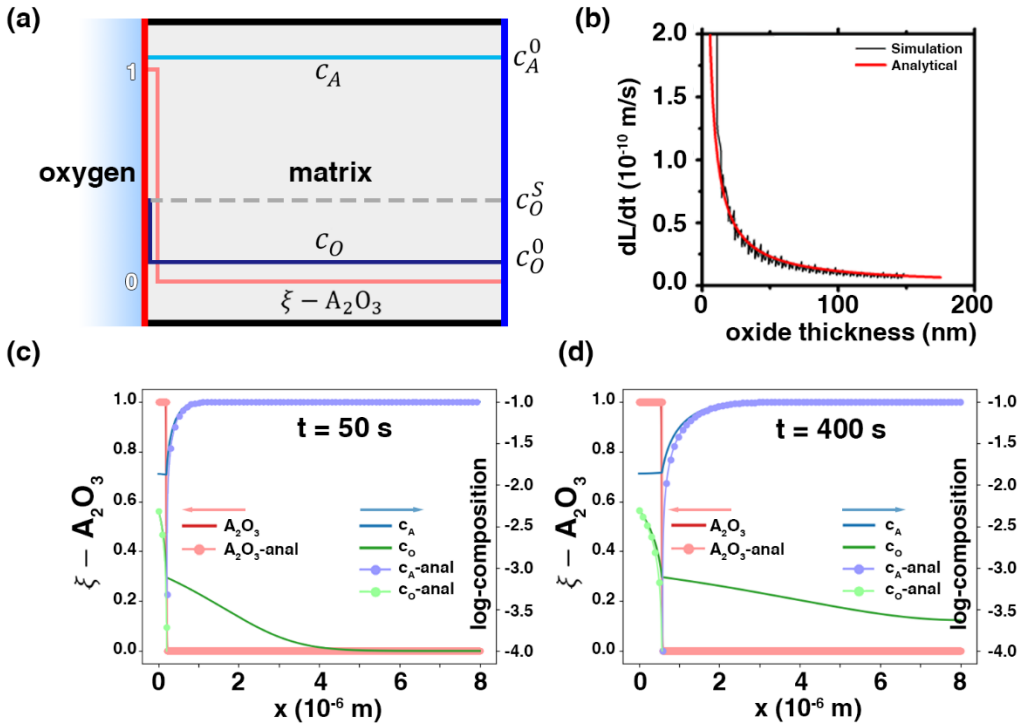

Figure 3: Simulation results compared with Wagner's theory. (a) Initial setup in an A-B alloy with A the only reactive component with oxygen, the initial composition of A is uniform while the composition of oxygen is initially depleted. The order parameter ξ representing the oxide A_2O_3 is finite only within 10 nm near the oxygen-material interface. (b) the oxide thickness growth rate dL/dt with respect to oxide thickness L plot in the simulation compared with the analytical results

by Wagner's theory. (c)-(d), the A_2O_3, c_A and c_O profiles compared with analytical results by Wagner's theory at t=50 s and t=400 s, respectively.

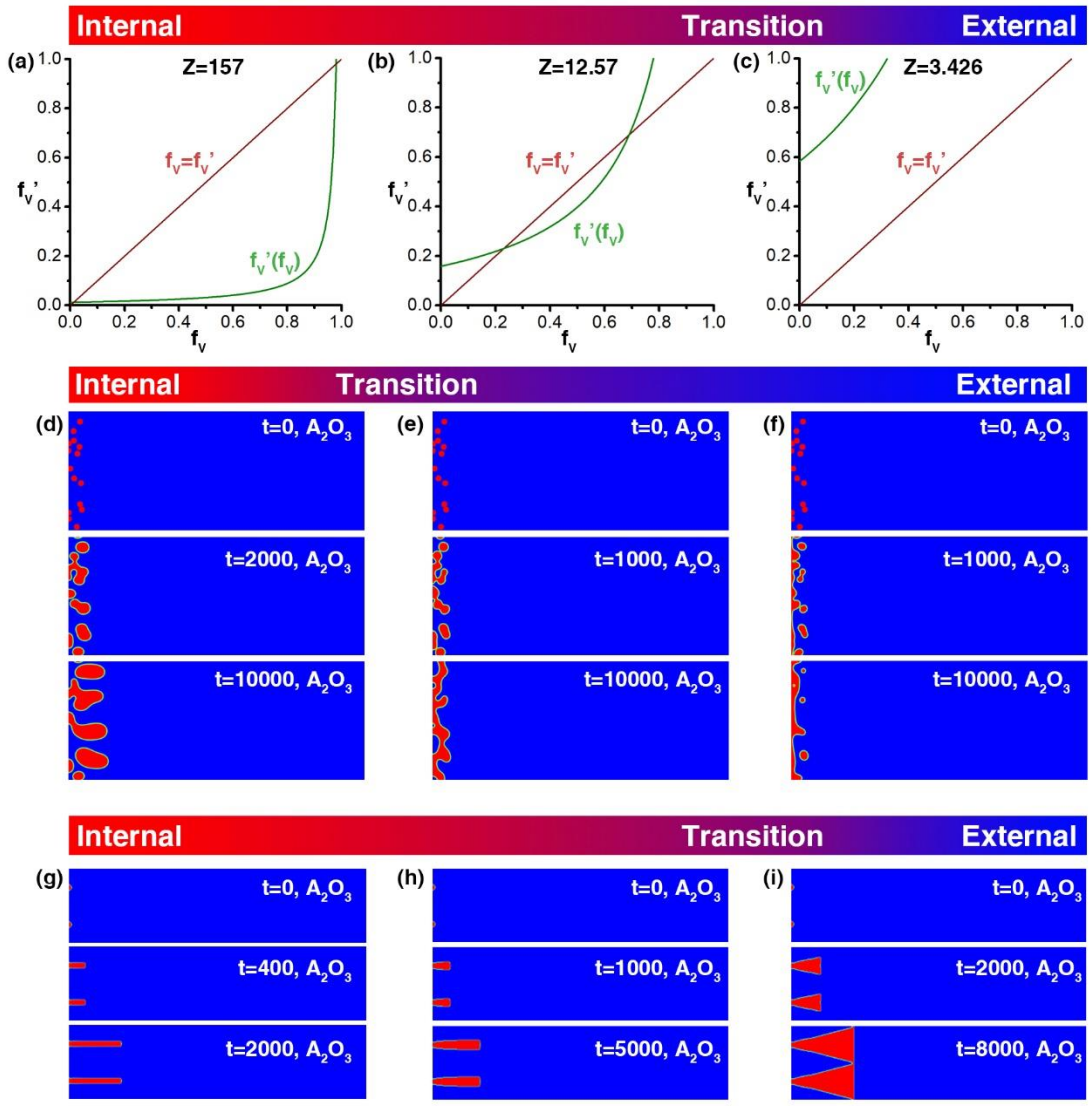

Figure 4: Oxidation results of the phase-field model comparing with Zhao's analytical model. (a)-(c) The prediction of oxidation results by Zhao's analytical model using different Z values (i.e., different diffusivities and initial compositions). (d)-(f) evolutionary profiles of A_2O_3 (red) by the phase-field model using the parameters specified in (a)-(c), respectively. (g)-(i) evolutionary

profiles of A_2O_3 (red) by the phase-field model with the assumption of blocking the diffusion of A inside the internal oxidation zone.

3.2 Model comparison with higher dimensional analytical models

More useful information can be collected from high-dimensional analytical model for oxidation with respect to the evolution of the internal oxidation zone, especially the morphological factors. Meanwhile, however, more assumptions should be made in order to reach an explicit and reliable solution in such an analytical model. A notable analytical model for oxidation in 2D and 3D is proposed by Zhao *et al*. [23]. In Zhao's model, the diffusivity of oxygen is varied as a function of the oxide volume fraction in the internal oxidation zone, in contrast to the constant oxygen diffusivity in Wagner's model. The effective diffusivity of oxygen is expressed by

$$D_O^{eff} = D_O^0 \cdot \frac{2(1-f_V)}{2+f_V} \tag{7}$$

which is obtained by fitting experimental measurements.

By using Equation (7), and solving the couple-flux equation in a manner similar to the Wagner's model, Zhao *et al*. quantitatively derived how the oxide volume fraction f_V in the internal oxidation zone would change during the oxidation process, instead of being a constant as in Wagner's theory. The evolution of f_V is described by a recursion equation of f_V:

$$f_V' = \frac{\nu}{\nu + \left(Z \cdot \frac{1-f_V}{2+f_V} - 1\right)} \tag{8}$$

where f_V and f_V' represent the volume fraction of the oxidation front and the newly forming oxide layer, respectively, $\nu = V_m^{oxide}/V_m^{matrix}$ is the ratio of the molar volume of the oxide and the matrix. Equation (8) reveals a quantitative relationship between the evolution of f_V and parameter

Z, where $Z = \frac{2\pi c_S D_O^0}{3D_A (c_A^0)^2}$ for the proposed oxide A_2O_3. That is, the coefficient Z is related to surface composition of oxygen c_S, initial composition of A in the matrix c_A^0 as well as the diffusivities D_A and D_O in the matrix. As the next step, the relative location between the curves $f_V'(f_V)$ based on Equation (8) and the line $f_V' = f_V$ is analyzed, as shown in Figures 4 (a)-(c). In these plots, we choose three different sets of material parameters with decreasing Z values representing the situations of internal oxidation, transition states, and external oxidation, respectively. When Z is large, the curve $f_V'(f_V)$ for Equation (8) would intersect with line $f_V' = f_V$ at the point $(f_V^\star, f_V^\star)$, which indicates a steady columnar growth with an equilibrium volume fraction $f_V^\star$, as shown in Figure 4 (a). On the other hand, when Z is small and there are no intersections between the curve $f_V'(f_V)$ and the line $f_V' = f_V$, the recursion Equation (8) would lead to an increasing f_V until it reaches unity, as shown in Figure 4 (c). Therefore, the recursion of Equation (8) results in two distinctive oxidation morphologies: an eventually continuous layer with $f_V = 1$ or a steady state growth internal oxide layer with $f_V = f_V^\star$. It should be noted that Equation (8) is valid only when $c_S/c_A^0 \ll D_A/D_O \ll 1$ [14]. That is, the parameters should be carefully chosen while adopting the analytical model.

Next, we employ our phase-field model using the same parameters as in Figures 4 (a)-(c), and we plot the corresponding oxide evolutionary profiles in Figures 4 (d)-(f). The simulation results indicate that the predictions by our phase-field model are qualitatively consistent with Zhao's analytical model while notable differences exist. Similar to the analytical predictions, our phase-field model predicts a clear transition from internal oxidation to external oxidation as Z decreases based on the same sets of parameters. However, two outstanding differences can be noticed: (1) After comparing Figures 4 (a) and (d), the steady state oxide volume fraction $f_V^\star$ is significantly different as Zhao's model predicts that $f_V^\star$ is less than 0.1 while our phase-field model shows that

$f_V^\star \approx 0.6$, which is much larger; (2) In terms of parameter Z, it is easier to form a continuous layer in the phase-field model compared with Zhao's analytical model. The main reasons for these differences include the assumptions in the analytical models, the deviation of $D_O^{eff} - f_V$ relation as well as the effect of shape and distribution of oxide nuclei. Among these reasons, the assumption of an IOZ is of pivotal importance, as the analytical model prohibits reactions and diffusion of A inside IOZ, while the diffusion of oxygen is allowed. In Figures 4 (g)-(i), we examine the influence of the IOZ assumption by blocking the diffusion of A within IOZ artificially. As the initial condition, regular initial oxide nuclei with the semi-circle shape are added at the oxygen-material interface (left). During the evolution, the oxide would grow to the matrix (right) with a straight internal oxidation front (IOF) line. The simulation results show great consistency with those from the analytical model, indicating the importance of the IOZ assumption on the analytical model and how this would modify the prediction in the phase-field model. A detailed analysis to the other factors that may result in the discrepancy between the two models is discussed in Section 4.2.

It should be noted that Zhao's analytical model cannot be applied to some practical cases as the prerequisite $c_S/c_A^0 \ll D_A/D_O \ll 1$ is not valid in some alloy systems with certain combinations of oxygen partial pressure and initial A compositions, and thus an explicit recursive $f_V - f_V'$ relation may not exist. On the other hand, our phase-field model gives consistent and continuous predictions on the evolutionary profiles regardless of the prerequisite, and one series of simulations are shown in Figure 5, where we only change the magnitude of initial A composition c_{A}^0. The simulation results clearly show the transition from internal oxidation to external oxidation as the initial A composition increases. These simulations may be of experimental interests as they help design alloy systems that endure oxidation with minimum A composition at certain working conditions.

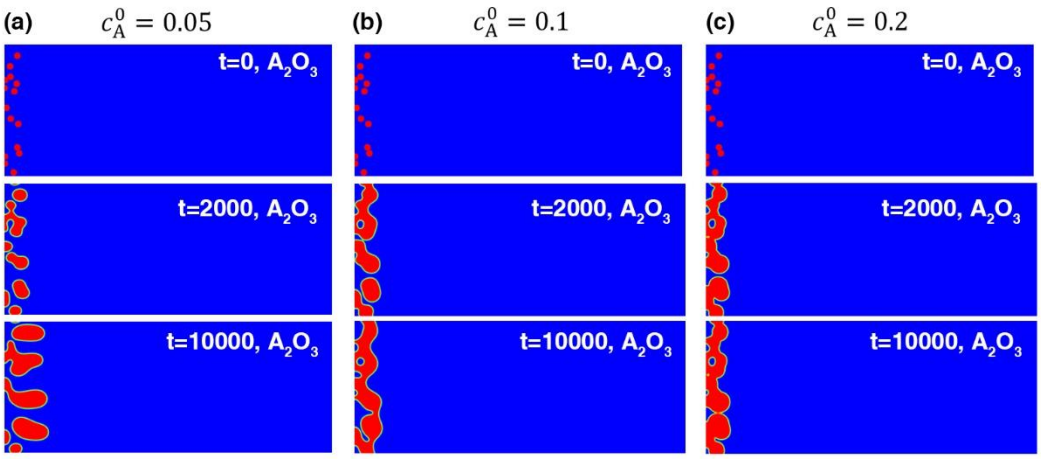

Figure 5: Phase-field simulation results for 2D system with initial round oxide nuclei randomly distributed near the matrix-oxygen interface (left bound of the simulation box) for (a) $c_A^0 = 0.05$, (b) $c_A^0 = 0.1$, (c) $c_A^0 = 0.2$, respectively.

4 Discussions

In Section 3.2, we compared the simulation results from our phase-field model with those from the analytical model by Zhao *et al*. The results are qualitatively consistent while quantitative differences exist in the critical Z value which tells apart internal and external oxidation, as well as in the steady state oxide volume fraction $f_V^\star$ when a steady internal oxidation process is predicted in both models. Here we investigate the origin of the discrepancies between our phase-field model and Zhao's analytical model in detail.

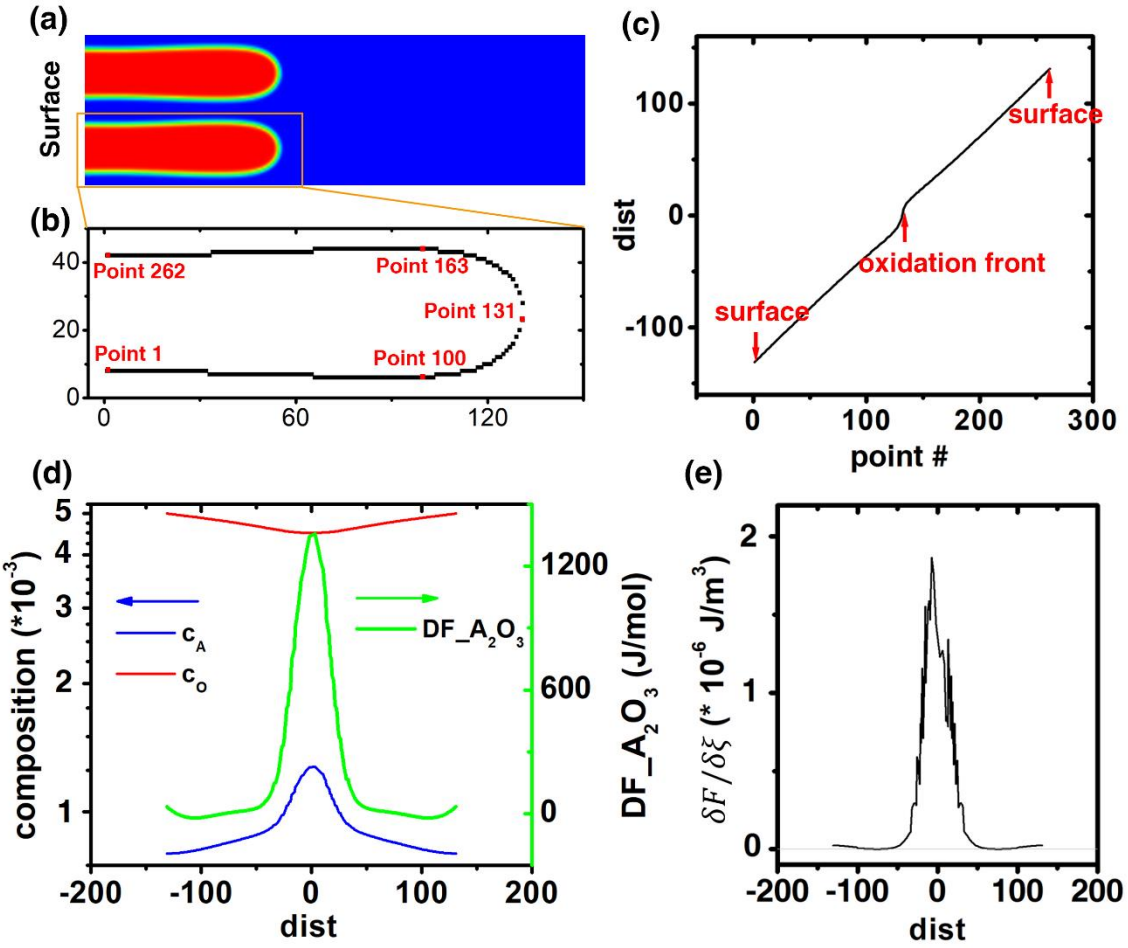

Figure 6: Driving force analysis of a representative time frame at t=27000 s during the oxidation process. (a) Oxidation profile t=27000 s showing two oxide particles (red) in a matrix (blue). (b) The sequential interfacial points determined by an isosurface tracking approach. (c) Interfacial point number as a function of weighed distance between the point and the point of oxidation front. (d) A and O compositions and reaction driving force as functions of weighed distance. (e) overall driving force $\delta F/\delta\xi$ as a function of weighed distance.

4.1 The evolution of the internal oxidation zone

One of the most outstanding differences between our phase-field model and Zhao's analytical oxidation model is the treatment of oxidation process inside the IOZ. In Zhao's model, the reaction

process is only allowed at the internal oxidation front (which possesses zero thickness) and frozen inside the IOZ. In our phase-field simulation, the driving force for oxidation process at every mesh point in the material system is calculated by the chemical potential difference between the reactants and the product, so the oxidation reaction is allowed at any oxide-matrix interfaces as long as there are sufficient reactants supplies.

To examine whether oxidation can happen and evaluate possible oxide growth direction (lateral vs. horizontal) inside the IOZ, the oxidation reaction driving force is analyzed along the oxide-matrix interfaces using an isosurface tracking approach based on the value of ξ. Figure 6 shows the driving force analysis for a simulation with surface oxygen composition $c_s = 0.005$ and initial A composition $c_A^0 = 0.05$. Figures 6(a) and 6(b) show the A_2O_3 morphology and the corresponding interfacial mesh points tracked for the bottom oxide particle at *t*=27000 s, respectively. In order to visualize the driving forces and fields in a 1D plot, we calculate the distances between all the points on the isosurface and the center of the isosurface (i.e., point 131 in Figure 6 (b) and also the internal oxidation front), and assign a negative weighed distances ("*dist*") to the points whose y value is smaller than that of the isosurface center. Figure 6 (c) plots the weighed distances ("*dist*") versus point indices, and the compositions and reaction driving force are plotted in Figure 6 (d). It shows a smaller oxygen composition and a larger A composition at internal oxidation front compared with those at the gas-material interface. Although the reaction driving force reaches its maximum at the oxidation front, its value inside the IOZ is still significant that cannot be neglected. According to Figure 6 (e), the overall driving force, which can be obtained by dividing oxidation rate $d\xi/dt$ by coefficient L_ξ, is significant for the points with -50<*dist*<50 despite a sharp decrease of the driving force at $|\mathrm{dist}| \approx 30$. This indicates a small yet important lateral (side) growth rate during the oxidation process, which could determine whether

a continuous oxide film can form. Moreover, when the oxide volume fraction is small, e.g., in the initial stages of the oxidation process upon nuclei form near the oxygen-matrix interface, the ratio between lateral growth rate and horizontal growth rate is significantly larger than that of larger volume fractions (see supplemental material for details), and it reaches nearly unity when $f_V < 0.4$. This leads to the conclusion that the steady state oxide volume fraction in IOZ must be larger than 0.4 based on the phase-field simulation since the blocking effect of IOZ is not significant when $f_V < 0.4$. Therefore, the oxidation reaction inside IOZ should not be neglected.

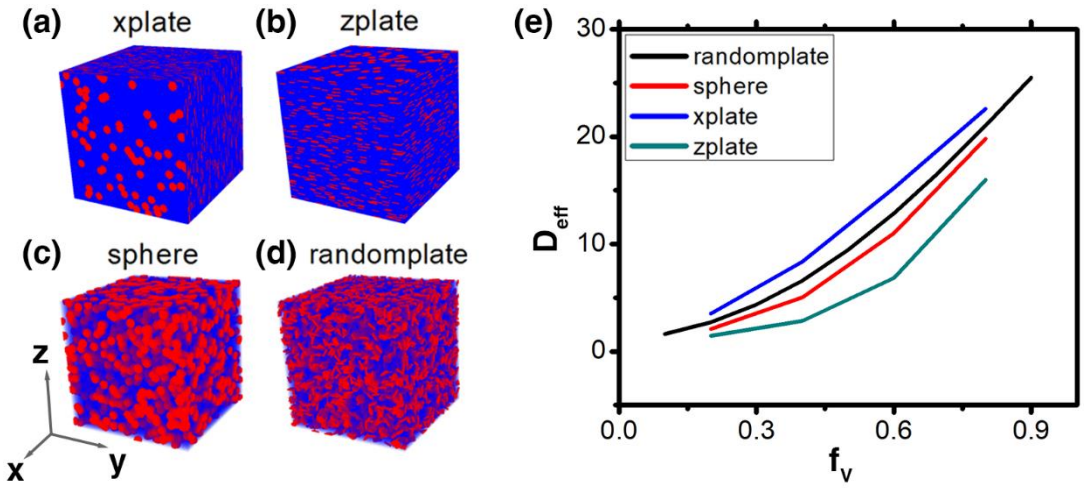

Figure 7: Effective diffusivity as functions of oxide volume fraction f_V with different oxide nuclei shapes and distributions. (a)-(d) Different initial setups of oxides with disk shape perpendicular to x axis, disk shape perpendicular to z axis, spherical shape, disk shape with randomized directions, respectively. (e) Effective diffusivity as a function of f_V using different set-ups in (a)-(d).

4.2 The effect of nuclei shape and distribution

In Zhao's analytical model, the expression of the effective diffusivity of oxygen D_O^{eff} as a function of f_V (i.e., Equation (7)) is crucial in determining the recursive Equation (8) and hence the resultant oxidation kinetics. However, the expression used in Zhao's model does not take into account the shape and distribution effects of oxide particles. To examine these effect, the effective diffusivity is evaluated in the phase-field framework by solving the steady-state diffusion equation with different oxide particle shapes and orientations as shown in Figure 7. Figures 7 (a)-(d) show the initial setup with disk-like oxides (red) with its normal parallel to x/z axis, spherical particles, and randomized orientations, respectively, in a system with nx×ny×nz=400×400×400 grids. Figure 7 (e) shows the effective diffusivity measured along the x axis as a function of the oxide volume fraction f_V. The effective diffusivity is clearly different for different oxide shapes and orientation for the same f_V, which is contrary to the expression used in the analytical model where the effective diffusivity is only a function of f_V. It should be noted that the simulations shown in Figure 7 are three-dimensional (3D), and the results are qualitatively consistent with those in 2D simulations, see supplemental material for a detailed comparison of $D_{eff} - f_V$ relations between 2D and 3D.

The model is further applied to simulate the oxidation processes with preset nuclei of identical shape but different orientations, as shown in Figure 8. Two simulations are designed with triangular nuclei initially aligned in the middle of the matrix, with the tips of nuclei in Figure 8 (a) pointing to the oxygen-matrix interface while those in Figure 8 (b) pointing to the matrix. The simulation results in Figures 8 (c) and (d) show different oxidation morphologies as the case starting from Figure 8 (a) remains separate particles while the case of Figure 8 (b) forms a continuous layer. This indicates that local driving forces for oxidation reaction may change based

on either the local nuclei shape or distribution, resulting in differences in morphological evolution and the connectivity of the oxide. These results confirm the significant role of nuclei shape and distribution in the later stage oxide morphology.

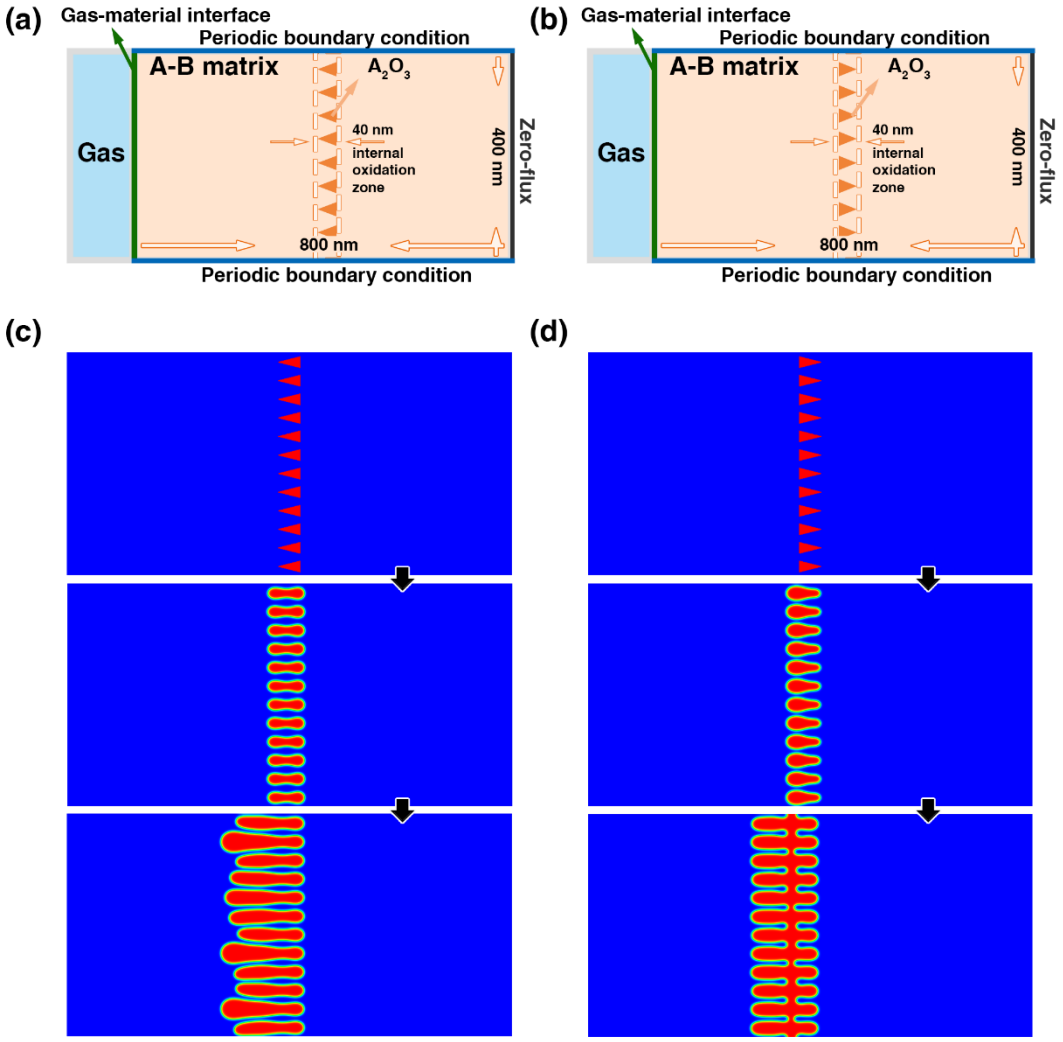

Figure 8: Simulation results for different A_2O_3 nuclei orientations. (a) and (b) Schematic plots for the initial setup for the triangular nuclei with tip pointing to the oxygen-matrix interface and to the matrix, respectively. (c) and (d) Evolutionary profiles for (a) and (b), respectively.

5 Summary

In this work, we developed a phase-field model to study the alloy oxidation at high temperatures. The model is validated against Wagner's theory using one-dimensional simulations. Two-dimensional simulations are then performed to study alloy oxidation in which the morphology of the oxides and its dependence on the effective diffusivity are discussed. Based on the phase-field simulation results, we examined the assumptions made by Wagner's and Zhao's analytical models. While the analytical models assume zero-thickness for the reaction front, the reaction occurs in a much broader region in our phase-field model including inside the internal oxidation zone. Eliminating the idealized assumption of zero thickness reaction front is an important step toward a more quantitative understanding on the kinetics of internal oxidation and especially its transition to external oxidation. The shape and distribution of oxide nuclei are also studied. It is shown to be crucial in determining the subsequent microstructure evolution in the oxidation processes. The phase-field model is applicable to modeling the microstructure-level oxidation kinetics, and especially internal oxidation and its transition to external oxidation in a general multicomponent alloy and thus can be employed to understand the microstructure-level alloy oxidation mechanisms.

Acknowledgement

This project is supported in part by an appointment to the Internship/Research Participation Program (RW) at the National Energy Technology Laboratory, US Department of Energy, administered by the Oak Ridge Institute for Science and Education. RW and LQC are partially supported by the National Science Foundation (NSF) grant number DMR-1744213. The research was executed through NETL Research & Innovation Center's eXtremeMAT FWP coordinated by

David Alman. The simulations were supported by the Extreme Science and Engineering Discovery Environment (XSEDE), which is supported by the National Science Foundation under Grant ACI-1548562. The authors acknowledge helpful discussions with Professor Brian Gleeson (U. Pitt), Drs. Mike Brady (ORNL), Laurent Capolungo (LANL), Jeff Hawk (NETL), and David Alman (NETL).

Disclaimer

References

[1] E. Airiskallio, E. Nurmi, M. Heinonen, I. Väyrynen, K. Kokko, M. Ropo, M. Punkkinen, H. Pitkänen, M. Alatalo, J. Kollár, High temperature oxidation of Fe–Al and Fe–Cr–Al alloys: The role of Cr as a chemically active element, Corrosion Science 52(10) (2010) 3394-3404.

[2] E. Essuman, G. Meier, J. Żurek, M. Hänsel, L. Singheiser, W. Quadakkers, Enhanced internal oxidation as trigger for breakaway oxidation of Fe–Cr alloys in gases containing water vapor, Scripta materialia 57(9) (2007) 845-848.

[3] T. Gheno, D. Monceau, D.J. Young, Mechanism of breakaway oxidation of Fe–Cr and Fe–Cr–Ni alloys in dry and wet carbon dioxide, Corrosion Science 64 (2012) 222-233.

[4] Y. Gong, D. Young, P. Kontis, Y.-L. Chiu, H. Larsson, A. Shin, J. Pearson, M. Moody, R. Reed, On the breakaway oxidation of Fe9Cr1Mo steel in high pressure CO_2, Acta Materialia 130 (2017) 361-374.

[5] G.H. Meier, K. Jung, N. Mu, N.M. Yanar, F.S. Pettit, J.P. Abellán, T. Olszewski, L.N. Hierro, W.J. Quadakkers, G.R. Holcomb, Effect of alloy composition and exposure conditions on the selective oxidation behavior of ferritic Fe–Cr and Fe–Cr–X alloys, Oxidation of Metals 74(5) (2010) 319-340.

[6] K. Messaoudi, A. Huntz, B. Lesage, Diffusion and growth mechanism of Al2O3 scales on ferritic Fe-Cr-Al alloys, Materials Science and Engineering: A 247(1-2) (1998) 248-262.

[7] A. Velon, I. Olefjord, Oxidation behavior of Ni3Al and Fe3Al: II. Early stage of oxide growth, Oxidation of Metals 56(5-6) (2001) 425-452.

[8] N. Birks, G.H. Meier, F.S. Pettit, Introduction to the high temperature oxidation of metals, Cambridge university press2006.

[9] C. Giggins, F. Pettit, Oxidation of Ni-Cr-Al Alloys Between 1000 and 1200 C, Journal of the Electrochemical Society 118(11) (1971) 1782-1790.

[10] A.H. Heuer, D.B. Hovis, J.L. Smialek, B. Gleeson, Alumina scale formation: a new perspective, Journal of the American Ceramic Society 94 (2011) s146-s153.

[11] R. Prescott, M. Graham, The formation of aluminum oxide scales on high-temperature alloys, Oxidation of metals 38(3-4) (1992) 233-254.

[12] E. Schmucker, C. Petitjean, L. Martinelli, P.-J. Panteix, B. Lagha, M. Vilasi, Oxidation of Ni-Cr alloy at intermediate oxygen pressures. II. Towards the lifetime prediction of alloys, Corrosion Science 111 (2016) 467-473.

[13] E. Schmucker, C. Petitjean, L. Martinelli, P.-J. Panteix, S.B. Lagha, M. Vilasi, Oxidation of Ni-Cr alloy at intermediate oxygen pressures. I. Diffusion mechanisms through the oxide layer, Corrosion Science 111 (2016) 474-485.

[14] C. Wagner, Reaktionstypen bei der Oxydation von Legierungen, Zeitschrift für Elektrochemie, Berichte der Bunsengesellschaft für physikalische Chemie 63(7) (1959) 772-782.

[15] F. Pettit, Oxidation mechanisms for nickel-aluminum alloys at temperatures between 900℃ and 1300 C, Transactions of the Metallurgical Society of AIME 239 (1967) 1296-1305.

[16] A. Atkinson, Transport processes during the growth of oxide films at elevated temperature, Reviews of Modern Physics 57(2) (1985) 437.

[17] H. Atkinson, A review of the role of short-circuit diffusion in the oxidation of nickel, chromium, and nickel-chromium alloys, Oxidation of Metals 24(3-4) (1985) 177-197.

[18] P.Y. Hou, Impurity effects on alumina scale growth, Journal of the American Ceramic Society 86(4) (2003) 660-68.

[19] N. Cabrera, N.F. Mott, Theory of the oxidation of metals, Reports on progress in physics 12(1) (1949) 163.

[20] T.-L. Cheng, Y.-H. Wen, Toward a quantitative understanding of the electric field in thermal metal oxidation and a self-consistent Wagner theory, The journal of physical chemistry letters 5(13) (2014) 2289-2294.

[21] T.-L. Cheng, Y.-H. Wen, J.A. Hawk, Diffuse-Interface Modeling and Multiscale-Relay Simulation of Metal Oxidation Kinetics With Revisit on Wagner's Theory, The Journal of Physical Chemistry C 118(2) (2014) 1269-1284.

[22] Q. Sherman, P.W. Voorhees, Phase-field model of oxidation: Equilibrium, Physical Review E 95(3) (2017) 032801.

[23] W. Zhao, Y. Kang, J.M.A. Orozco, B. Gleeson, Quantitative approach for determining the critical volume fraction for the transition from internal to external oxidation, Oxidation of Metals 83(3) (2015) 187-201.

[24] K. Kim, Q.C. Sherman, L.K. Aagesen, P.W. Voorhees, Phase-field model of oxidation: Kinetics, Physical Review E 101(2) (2020) 022802.

[25] L.-Q. Chen, Phase-field models for microstructure evolution, Annual review of materials research 32(1) (2002) 113-140.

[26] A.T. Fromhold, THEORY OF METAL OXIDATION. I. FUNDAMENTALS, North-Holland, Amsterdam (1976).

[27] Y. Ji, Phase-Field Modeling of Precipitation in Metallic Alloys: Morphology, Kinetics and Hardening Effects, Pennsylvania State University, 2018.

[28] Y. Ji, L.-Q. Chen, Phase-Field Model of Stoichiometric Compounds and Solution Phases, Acta Materialia 234 (2022) 118007.

[29] R. Wang, Y. Ji, T. Cheng, F. Xue, L.-Q. Chen, Y.-H. Wen, A Phase-Field Study on Internal to External Oxidation Transition in High-Temperature Structural Alloys, JOM 74(4) (2022) 1435-1443.

[30] A.J. Ross, Solubility of Oxygen and Hydrogen and Diffusivity of Oxygen in the fcc Phase of the Al-fe-ni-ho System with Application to the Formation of a Protective α-al2o3 Scale at High Temperatures, The Pennsylvania State University (2015).

[31] F. Elrefaie, W. Smeltzer, Thermodynamics of Nickel-Aluminum-Oxygen system between 900 and 1400 K, Journal of the Electrochemical Society 128(10) (1981) 2237.

[32] A. Chatterjee, S. Srikanth, S. Sanyal, L. Krishna, K. Anand, P. Subramanian, Kinetic modeling of high temperature oxidation of Ni-base alloys, Computational Materials Science 50(3) (2011) 811-819.

Graphical Abstract

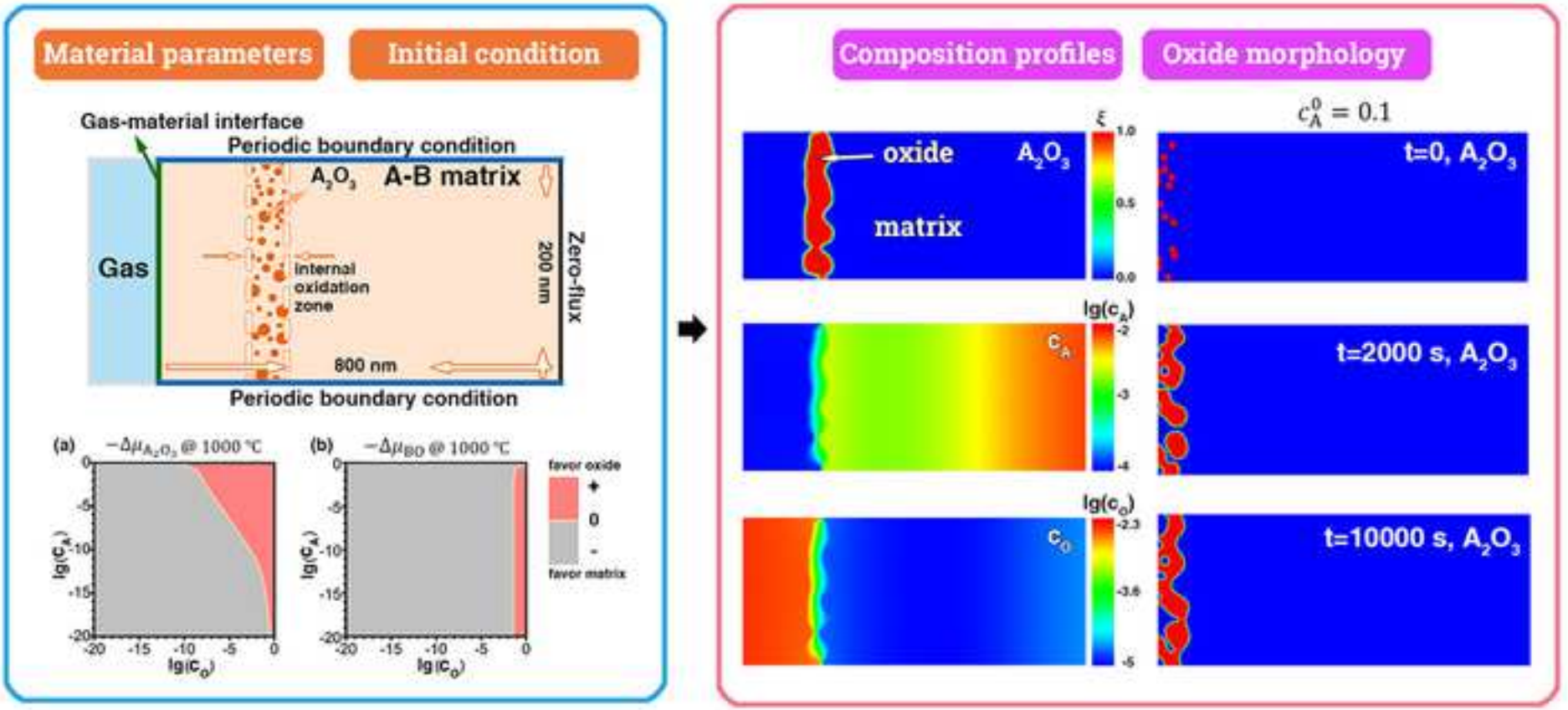

Declaration of interests

☒ The authors declare that they have no known competing financial interests or personal relationships that could have appeared to influence the work reported in this paper.

☐The authors declare the following financial interests/personal relationships which may be considered as potential competing interests:
